行政院國家科學委員會補助專題研究計畫 ■ 成 果 報 告 □期中進度報告

利用摻雜之硒化鎵晶體產生兆赫波之研究

計畫類別：■個別型計畫　□整合型計畫
計畫編號：NSC 96－2923－M－009－001－MY3
執行期間： 96 年 08 月 01 日至 99 年 07 月 31 日

執行機構及系所：國立交通大學 電子物理系

計畫主持人：羅志偉
共同主持人：莊振益、吳光雄
計畫參與人員：古新安、朱韋臻

成果報告類型(依經費核定清單規定繳交)：□精簡報告　■完整報告

本計畫除繳交成果報告外，另須繳交以下出國心得報告：
□赴國外出差或研習心得報告
□赴大陸地區出差或研習心得報告
■出席國際學術會議心得報告
□國際合作研究計畫國外研究報告

處理方式：除列管計畫及下列情形者外，得立即公開查詢
□涉及專利或其他智慧財產權，□一年□二年後可公開查詢

中　華　民　國　99 年　08 月　11 日

中文摘要

關鍵詞: 超快光電技術、超快動力學、兆赫電磁輻射源、時析光激發-兆赫波探測兆赫波、非線性光學晶體、硒化鎵晶體、差頻產生

本計畫將尋找適當的元素摻雜於非線性半導體硒化鎵晶體中，以提高其產生兆赫波之效率。近來已有研究群利用硒化鎵晶體產生一可調波長之兆赫波幅射。也因為此種晶體在兆赫波波段吸收率較低，所以在眾多非線性光學晶體中最被看好的材料之一。不過其本身的均勻度及光學透明度，卻成為產生高功率兆赫波幅射之限制。因此，本計劃的目標在透過硫及碲元素之摻雜，同時配合尋找穩定的長晶條件，以得到一具有高均勻度、高機械強度、高透光率等特性之高品質非線性半導體摻硫硒化鎵及摻碲硒化鎵晶體，進而實現高功率之兆赫波幅射光源。

英文摘要

Keywords: THz, nonlinear optical crystals, GaSe crystals, difference frequency generation, dipole antenna, ultrafast dynamics

This proposal is intended to find the proper doping elements in nonlinear optical semiconducting crystals, GaSe, for high efficiency terahertz (THz) generation. Recently, the possibility for generating tunable terahertz based on GaSe crystals was demonstrated by experiments. GaSe possesses the lowest absorption in the terahertz range among the known nonlinear crystals. Therefore, the GaSe crystals are prospective for THz generation by nonlinear-optical conversions (difference frequency generation, DFG) and optical rectification. On the other hand, the conversion efficiency and the output power are limited by the crystal properties such as optical transparency and homogeneity. These drawbacks could be improved by introducing the chemical elements with various atomic radiuses in the pure GaSe crystals. In this proposal, it is planed to find the proper conditions for growing the large homogeneous GaSe:S and GaSe:Te crystals with lower absorption in THz region and enhance the efficiency of THz generation.

Content

1. Background

Recently, there is growing interesting in fields using terahertz (THz) waves, or T-rays, for spectroscopy, imaging, communications, signal processing, and quantum information. The prospects of T-rays applications could be imaged by the nice cover picture of Rensselear Magazine as shown in Fig. 1-1 [1]. Why do they call it "Next Rays"? In the viewpoint of safety, the T-rays will not cause harmful photoionization in biological tissues due to their low photon energies (4 meV@ 1THz, one millions times weaker than an x-ray photon). Moreover, numerous organic molecules have rotational and vibrational transitions which lead to strong absorption and dispersion in the region from GHz to THz. These characteristics are specific to the targets and enable T-rays fingerprinting. Therefore, T-rays are the wave of the future. In a pass decade, this previously hidden region of the electromagnetic spectrum has caught the imagination of scientists around the world.

Terahertz domain of electromagnetic radiation spectrum (approximately 15 μm – 10 mm or 0.03 – 20 THz) is located between mid IR and microwave range and remains comparatively low investigated. That is connected with technical and technological difficulties in creation of corresponded element base (radiating and detecting devices, lenses, filters, and etc.). On the other hand, terahertz radiation possesses a set of important for practical applications properties. For instance, it has higher penetrating power than optical

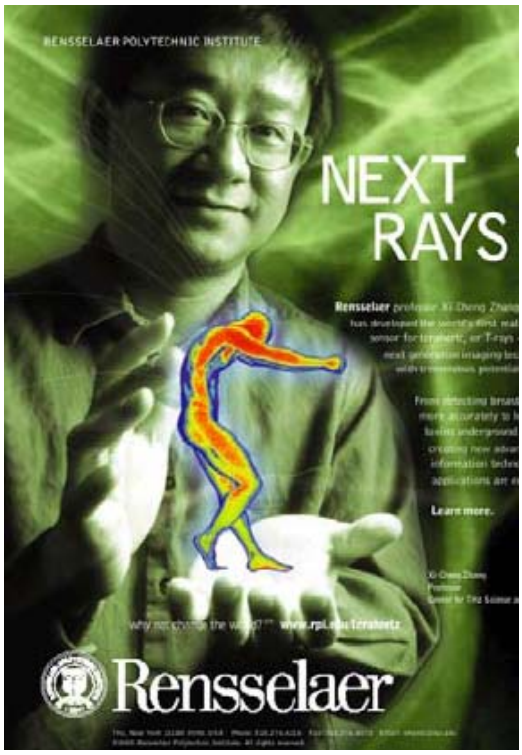

Fig. 1-1 The applications of THz are shown on the cover of Rensselear Magazine

radiation and allows more detailed imaging than microwaves. It can propagate through most of non-metallic and non-polar media. Many characteristic features of substances lie in this range, e.g. rotational and oscillating frequencies of molecules. On the base of THz radiation source, it is possible to create a remote detector for explosive substances with high spatial resolution. Terahertz spectroscopy becomes an important tool of molecular biology, electrophysics, medicine, and etc.

Early research concentrated on the generation and detection of THz radiation. By present time one can get terahertz radiation by dipole antennas [2-4], from semiconductor surface [5], by gas lasers with optical pump [6], free-electron lasers [7], and quantum-cascade lasers [8]. All methods have their merits and deficiencies. It is possible to obtain broad-band radiation with microwave lamps, but it is not coherent; free-electron lasers allow to get radiation in wide range and with high output power, but they are not compact and expensive thus being not available for most of research laboratories.

A way to create relatively compact and inexpensive coherent terahertz radiation source is to use the nonlinear optical conversion in nonlinear crystals. By the moment, the best results in terms of tuning range and output peak power are obtained on the GaSe and ZnGeP2 crystals [9, 10]. The tuning range of some thousands of micrometers and the peak power of some hundreds of watts were achieved. GaSe crystals have being grown since 1960s and possesses low mechanical properties due to it is layered and easy cleavable material, which makes a difficulty for growing long homogeneous crystals. In spite of its many attractive features for generation from near to mid infrared and further to terahertz range, the GaSe crystal is difficult to be cut and polished along some arbitrarily chosen directions. For the applications in optics, further improvement in the optical and mechanical properties of the GaSe crystals is highly desirable.

2. Goals

The doping of GaSe crystals seems to be the most economic way to radically improve its mechanical and other physical properties. In this project, we planed to find the conditions for growing the large homogeneous GaSe:Te and GaSe:S crystals with lower absorption in THz region. In order to figure out the influence of S and Te atoms in the GaSe crystals, we employ the THz time-domain spectroscopy to systematically study their physical and optical properties in THz range, e.g. the phonon modes, reflective index, and absorption coefficients. Additionally, we will prepare the GaSe:Te and GaSe:S crystals as the THz emitter and generate THz from these crystals by femtosecond laser pulses. Through the EO sampling method, the doping-dependent efficiency of THz generation could be clearly revealed. Finally, these results would further help the engineers to produce the high quality and more suitable doped GaSe crystals for THz generation and applications.

3. Results and discussions – in Russia side

3.1 Sample preparation

The GaSe:S and GaSe:Te crystals have been grown by the way of modified two-temperature method (horizontal variant) in Tomsk, Russia. The growth conditions are as follows,

- Growth rate is within 0.5-1 mm/hour.
- Melting temperature is within 1010-1020 ℃;
- Temperature gradient at the crystallization front is 10 degree/cm;

Specimens with thickness of 0.5 mm and 1.0 mm were made for investigation of physical properties and study of frequency conversion processes by exfoliation method from a grown single crystal boule. A few millimeters to few centimeters sized specimens were made by mechanical methods, e.g. diamond saw cutting and mechanical polishing. Then, they were fixed on the metal substrates with the aperture of 5 ~ 10 mm in diameter for preserving the flatness of specimens as shown in Fig. 3-1 and Fig. 3-2.

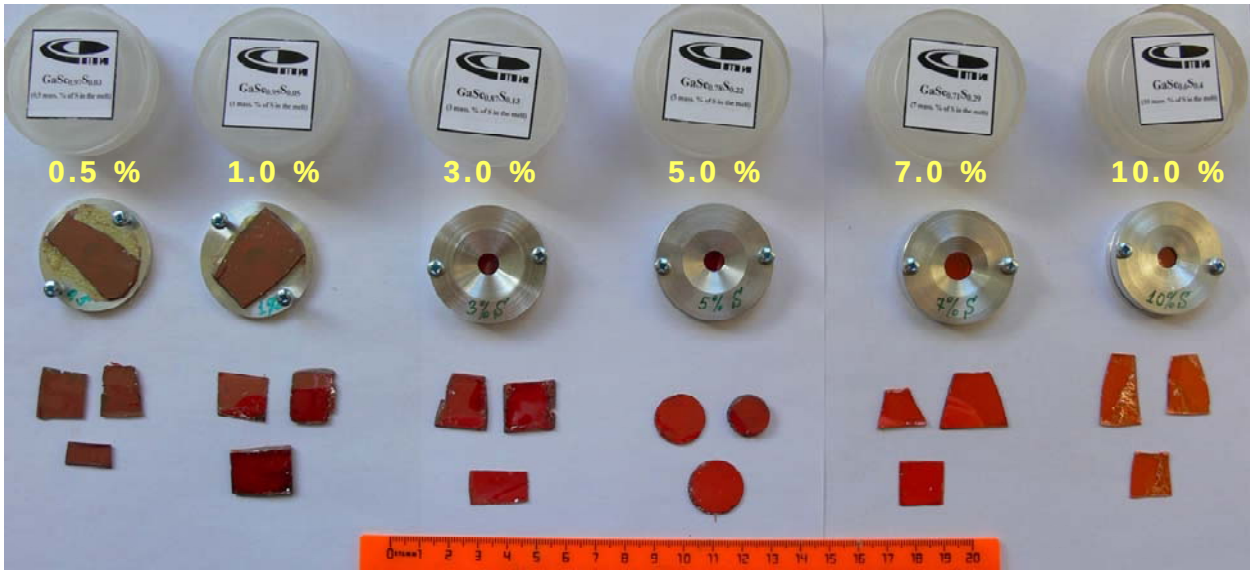

Fig. 3-1 External view of the GaSe:S samples with 0.5, 1.0, 3.0, 5.0, 7.0, 10.0 mass%.

Fig. 3-2 External view of the GaSe:Te samples with 0.05, 0.10, 0.50, 1.00, 2.00 mass%.

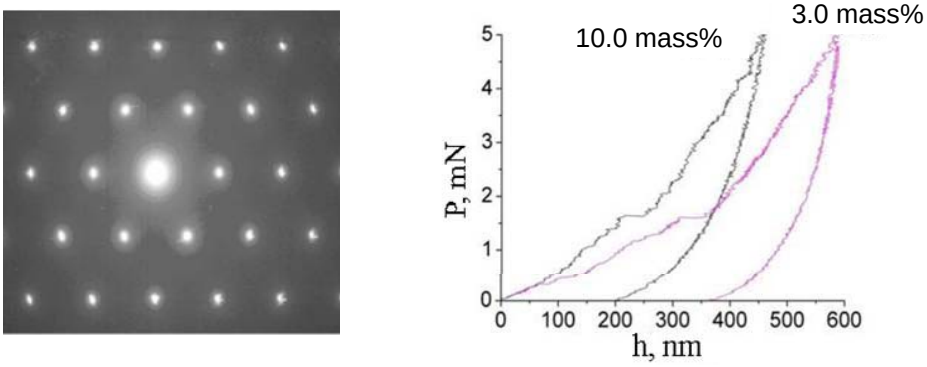

Fig. 3-3 (a) Electron diffraction pattern. (b) Loading diagrams for the surface parallel to the GaSe:S layers.

The crystallinity of GaSe:S crystals have been identified by the electron diffraction pattern which shows the hexagonal structure in ab-plane (see the Fig. 3-3(a)). Moreover, the bonding strength between the layers rises with increasing the content of sulfur as shown in Fig. 3-3(b). This means that the hardness of GaSe crystals was effectively enhanced by doping.

4. Results and discussions – in Taiwan side

4.1 Optical properties

The optical properties of GaSe:S and GaSe:S crystals have been measured by Raman spectroscopy and FTIR (Fourier Transform Infrared Spectroscopy) in Far-IR and Mid-IR region.

(i) GaSe:S crystals

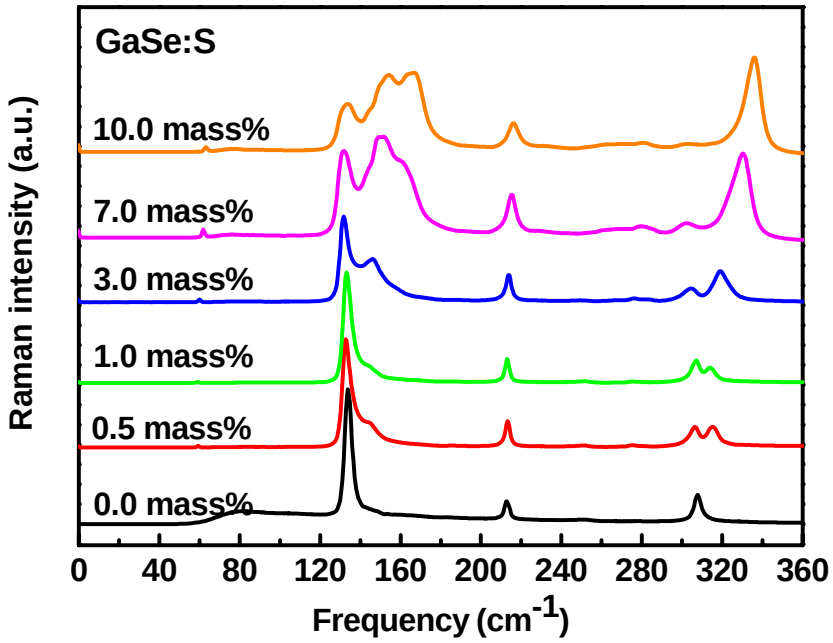

Fig. 4-1 Raman spectra in GaSe:S crystals.

For the pure GaSe crystals (0.0 mass%), there are three peaks at 134 cm^{-1}, 213 cm^{-1}, and 308 cm^{-1} in Raman spectra as shown in Fig. 4-1, which is consistent with Hayek's et al. results [11]. While increasing the concentration of sulfur in GaSe crystals, the peaks at 134 cm^{-1} and 308 cm^{-1} gradually shrink. On the contrary, the peak at 213 cm^{-1} gradually raises. Additionally, two new peaks at 145 cm^{-1} and 315 cm^{-1} would be induced by the S-doping even at very low sulfur concentration (e.g. 0.5 mass%). Besides, these two peaks monotonously shift to higher frequency as increasing the

content of sulfur. This means that the sulfur atom doped into the GaSe crystals would lead to the distortion of GaSe lattice and then reduce the phonon modes of the pure GaSe crystals. Meanwhile, the appearance of GaS compound further causes the new peaks at high frequency side of 134 cm^{-1} and 308 cm^{-1} peaks.

Figure 4-2 shows the transmission spectra of GaSe:S crystals from visible to far-IR. In the visible transmission spectra [see Fig. 4-2(a)], we clearly observed the shape edge around 0.62 μm which indicates the band gap of GaSe:S crystals. With increasing the concentration of S, the transmission edge shifts to the shorter wavelengths. This means the S-doping causes the larger band gap and thus changes the color from red to yellow. In mid-IR range, the transmission at wavelengths above 15 μm was strongly suppressed by the S-doping as shown in Fig. 4-2(b). On the contrary, the transmission at shorter wavelengths below 15 μm is no significant changes. These results imply that the heavy S-doped GaSe crystals are not suitable for mid-IR generation at wavelengths above 15 μm. In the far-IR range [Fig. 4-2(c)], the characteristics of transmission spectra are similar for the slightly S-doping ($\leqq$5.0 mass%) GaSe crystals. However, the deep at ~120 μm and the broad peak at ~200 μm are almost smeared in heavy S-doped ($\geqq$5.0 mass%) GaSe crystals due to the appearance of GaS compound evidenced from the Raman spectra in Fig. 4-1. Generally speaking, the transmission is very low between 22 μm and 70 μm to restrict the THz applications around this regime.

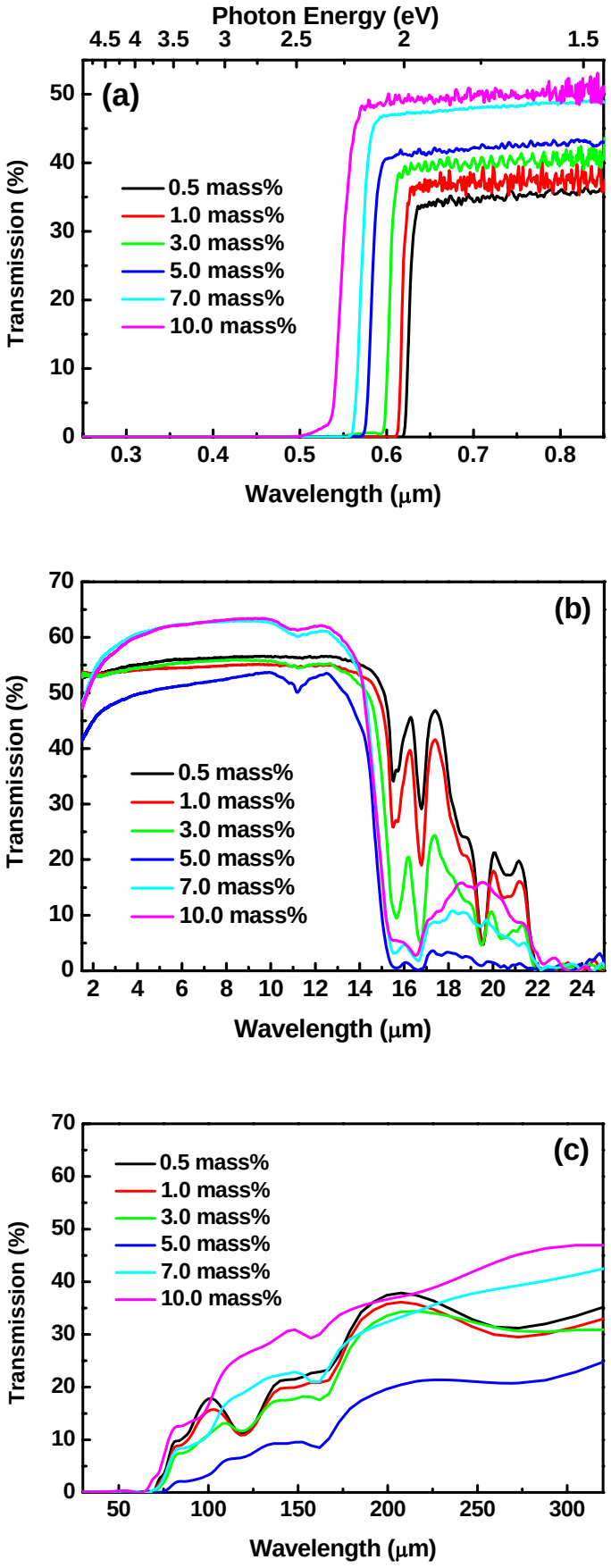

Fig. 4-2 Transmission spectra in various S-doped GaSe crystals.

(ii) GaSe:Te crystals

Figure 4-3 shows the Raman spectra in Te-doped GaSe crystals. In the range from 20 cm^{-1} to 360 cm^{-1}, the phonon modes for the cases of various Te-doping GaSe crystals are quite similar with the pure GaSe crystals which are totally different from the cases of S-doping in Fig. 4-1. This may be due to the rather slight Te concentration in GaSe crystals and without additional compounds related to Te.

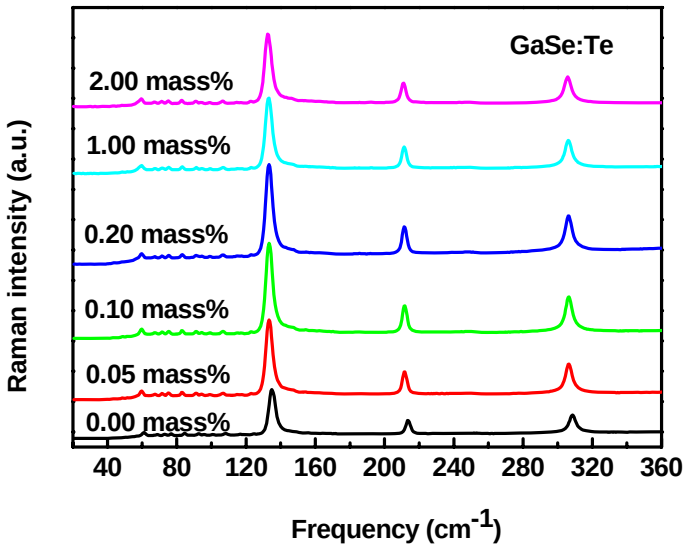

Fig. 4-3 Raman spectra in GaSe:Te crystals.

Following the same analysis in S-doped samples, the transmission spectra of GaSe:Te crystals were also performed from visible to far-IR range as shown in Fig. 4-4. The band gap of GaSe:Te crystals gradually decrease as increasing the concentration of Te according to the shift of transmission edge in Fig. 4(a) which is totally opposite to the S-doping. This may be resulted in the ionic size. For instance, the smaller size of S atom will cause the lattice distortion with compressive stress to increase the band gap. On the contrary, the larger size of Te atom will cause the lattice distortion with tensile stress to decrease the band gap. For the transmission spectra in mid-IR [Fig. 4-4(b)], there are no significant characteristic changes with varying the Te concentration. The most interesting thing is that the whole spectra increase at slightly Te-doped cases. This implies that it may be

possible to enhance the THz generation efficiency from 2 μm to 22 μm. Additionally, the same behavior was also found in far-IR range as shown in Fig. 4-4(c) which is possible to enhance the THz generation power in this range.

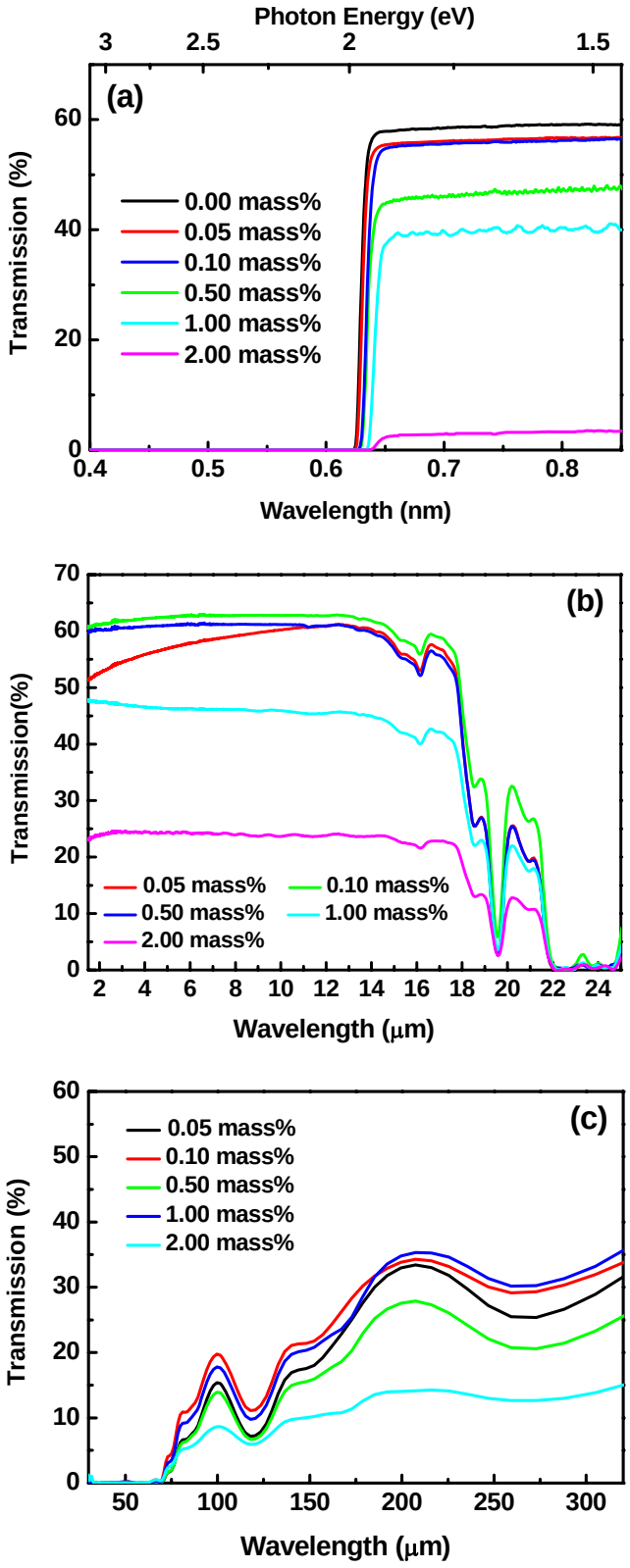

Fig. 4-4 Transmission spectra in various Te-doped GaSe crystals.

4.2 Terahertz time-domain spectroscopy measurements

A THz time-domain spectroscopy (THz-TDS) system with a focused beam at the position of a sample has been used in this study as shown in Fig. 4-5. The THz pulses, generated by femtosecond-laser-excited dipolelike antenna fabricated on semiconductor InP, were collimated by the off-axis paraboloidal mirror and focused on the sample by the other off-axis paraboloidal mirror. The spot size of the THz wave through the sample is about 4 mm in diameter which is smaller than the size of samples to increase the signal to noise ratio. The transmitted THz pulses were collected and focused on a (110)-oriented ZnTe crystal. The detection of THz wave using the free-space electro-optic sampling technique [12] was setup on a mode-locked Ti:sapphire laser operating at 800 nm (1.55 eV) with an 80 MHz train of 50 fs pulses. The entire setup was placed in an airtight enclosure purged with dry nitrogen and maintained at a relative humidity of < 5.0 % to avoid the strong absorption of water vapor in THz range.

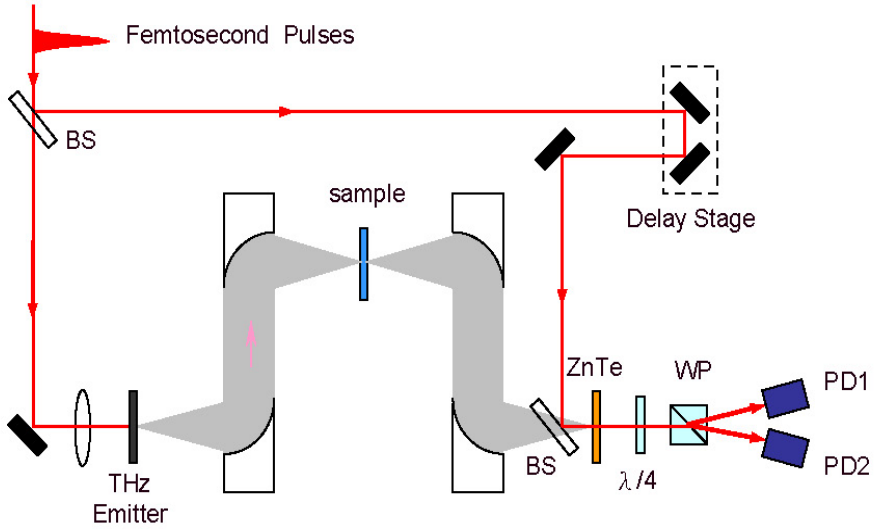

Fig. 4-5 Schematic of the THz-TDS. BS: Beam splitter. WP: Wollaston polarizer. DP1 and PD2: Photodiode 1 and photodiode 2, respectively.

Though THz-TDS measurements, temporal profiles can be got. The delay time (Δt) from a reference THz pulse is due to the thickness and the

refractive index of samples. From the measured delay time Δt, the group index of refraction is calculated by $ng = 1+c\Delta t/d$, where d is the thickness of samples, and c is the speed of light in vacuum. The refractive index at various frequencies (ν) is determined by the phase difference as $n(\nu)=1+c\Delta\theta/2\pi\nu d$, and the absorption coefficient is calculated as $\alpha(\nu)=-(1/d)\ln[\eta \cdot Ps(\nu, d)/Pr(\nu, d)]$ [13], where η is a correcting factor related to the reflection losses at the two crystal/air interfaces. $Ps(\nu, d)$ and $Pr(\nu, d)$ are the measured transmittances for sample and reference (without sample), respectively. Above analyses enabled the quite accurate determination of the refractive index $n(\nu)$ and power absorption $\alpha(\nu)$.

(i) GaSe:S crystals

The typical profiles of the THz pulses transmitted through the air and samples are shown in Fig. 4-6. After through the GaSe:S crystals, the THz pulses do not only shrink in amplitude but also delay in time. The time delay (Δt) from the reference THz pulse (the thick-solid line in Fig. 4-6) is due to the thickness and the refractive index of GaSe:S crystals. From the measured Δt, the group index of refraction is calculated by $n_g = 1+(c\Delta t/d)$, where d is the thickness of samples and c is the speed of light in vacuum. For the thinnest crystal (GaSe) with 600 μm, the $n_g = 3.22$, which is consistent with the values of the refractive index (n) in the main region from 0.7 to 1.2 THz at room temperature (see Fig. 4-7). In this study, the propagation direction of the incident THz beam is parallel with the optical axis. Thus, the refractive index measured in this geometry is the ordinary refractive index, n_o.

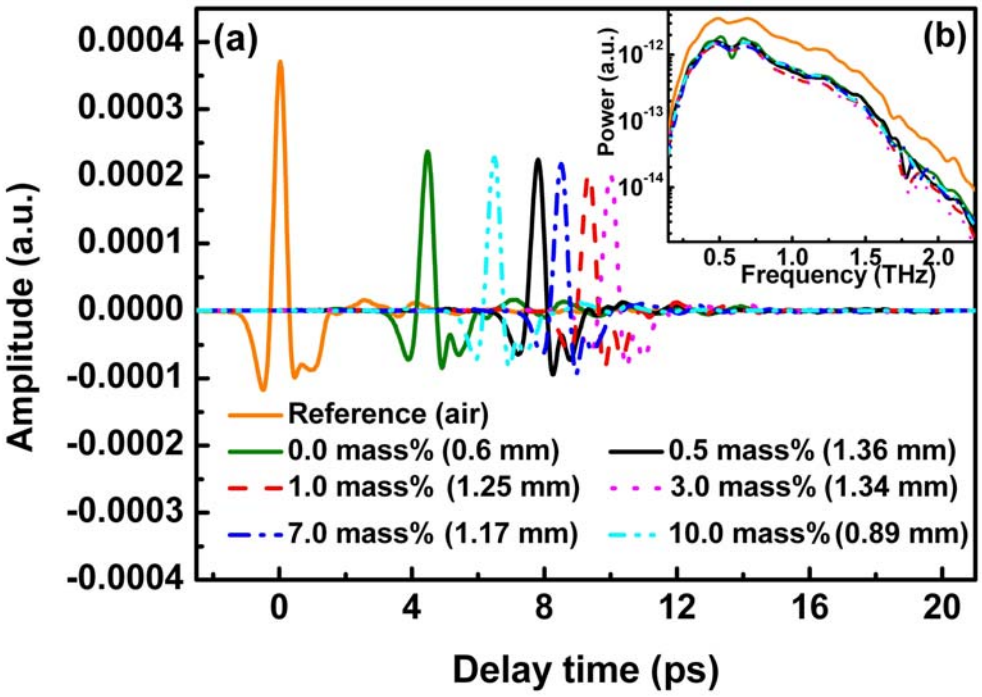

Fig. 4-6 (a) Temporal profiles of the THz pulse transmitted through GaSe:S crystals and air (thick-solid line). (b) The power spectra of the THz pulse transmitted through GaSe:S crystals and air (thick-solid line).

The inset of Fig. 4-6 shows the frequency spectra in THz range, which are directly transferred from the THz signal in time domain by Fast Fourier Transform method. In order to eliminate the modulation in the frequency spectra, the data analysis was only performed on the main pulse part before the second reflective pulse. The refractive index at various frequencies (ν) is determined by the phase difference as $n(\nu) = 1+(c\Delta\theta/2\pi\nu d)$, and the absorption coefficient is calculated as $\alpha(\nu) = -(1/d)\ \ln[\eta \cdot P_s(\nu, d) / P_r(\nu, d)]$ [13], where η is a correcting factor related to the reflection losses at the two crystal/air interfaces. $P_s(\nu, d)$ and $P_r(\nu, d)$ are the measured transmittances for a sample and a reference (without samples), respectively. Above analyses enabled the quite accurate determination of the refractive index $n(\nu)$ and absorption coefficient $\alpha(\nu)$ for the GaSe:S crystals as shown in Fig. 4-7 and Fig. 4-8, respectively.

The refractive index of the slightly S-doped GaSe crystals (GaSe:S, ≦ 3.0 mass%) is almost the same with that of GaSe crystals. For the heavy S-doped GaSe crystals, however, the refractive index is markedly smaller than that of GaSe and slightly S-doped GaSe crystals. These characteristics surprisingly match the evolution of carrier concentration with increasing the concentration of S as shown in Table I, which were measured from the Hall measurements. The carrier concentration almost keeps around 4×10^{15} cm^{-3} while the ≦3.0 mass% in GaSe:S but dramatically drops as >3.0 mass% due to the large substitution of Se atoms for the smaller atomic size of S [14]. Thus, the lightly amount of S atoms does not affect the crystal structure and the refractive index of GaSe:S. On the contrary, a large amount of S atoms which massively substitutes the Se atoms will form the GaS phase [15] to markedly shrink the crystal structure of GaSe:S and then leads the small index of refraction as shown in the dash-dotted and dash-dot-dotted lines in Fig. 4-7 due to the diminution of conductivity and the formation of GaS possessed lower refractive index [16, 17].

Although the refractive index in THz is insensitive to the concentration of S in the slightly S-doping region, the absorption coefficient spectra are strongly dependent on the doping of S. For pure GaSe crystals, a so-called rigid layer mode ($E'^{(2)}$) which moved as a rigid unit [18], is clearly observed at 0.585 THz in Fig. 4-8 and consistent with the results reported by Chen *et al*. [19]. For the S-doping GaSe crystals, however, this rigid layer mode becomes vague and the other phonon mode ($E''^{(2)}$) is clearly observed at high frequency range from 1.78 to 1.90 THz. Due to the substitution of Se atoms for the lighter S atoms, some lighter atomic sites appear in the layer unit-two Ga atoms and two Se atoms to destroy the rigid layer mode $E'^{(2)}$. Thus, the $E''^{(2)}$ phonon mode at ~ 1.78 THz performed by the atomic displacement

vector dominates the absorption coefficient spectra and shifts to high frequency region as increasing the concentration of S. Moreover, the peak intensity of $E''^{(2)}$ phonon mode is gradually suppressed when the concentration of S increases due to the formation of GaS phase at >3.0 mass%.

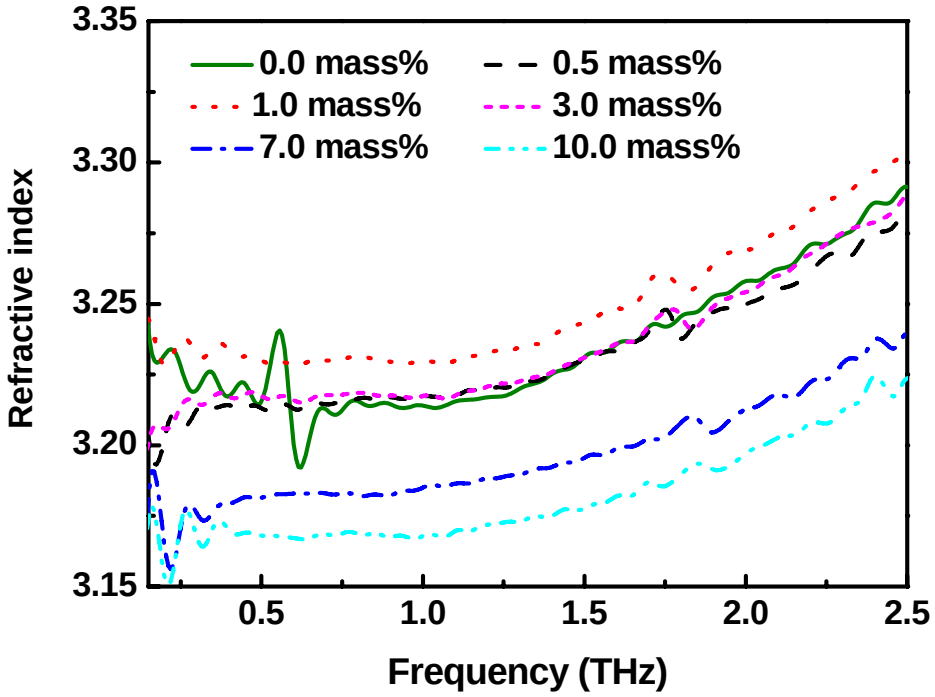

Fig. 4-7 Refractive index of the GaSe:S crystals in THz range.

Table I The results of Hall measurements in the GaSe:S crystals.

GaSe:S (mass%)	σ ($\Omega^{-1} \cdot cm^{-1}$)	μ ($cm^2/B \cdot c$)	P (cm^{-3})
0.0	1×10^{-2}~3.5×10^{-3}	19~22.5	$1\sim5\times10^{15}$
0.5	1.46×10^{-2}	23.2	3.94×10^{15}
1.0	1.72×10^{-2}	20.3	5.32×10^{15}
3.0	8.6×10^{-3}	15	3.6×10^{15}
7.0	9.79×10^{-4}	15.1	4×10^{14}
10.0	1.5×10^{-4}	8.9	1×10^{14}

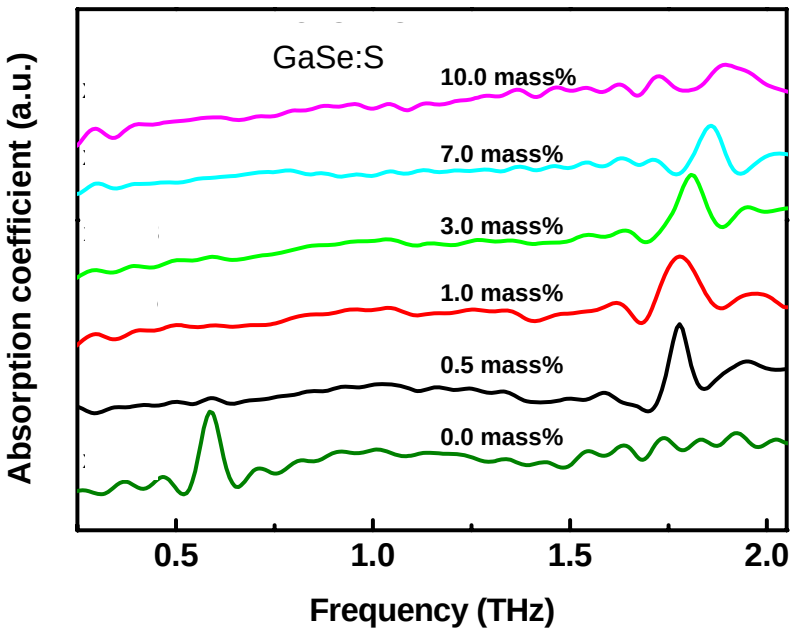

Fig. 4-8 Power absorption spectra of the GaSe:S crystals in THz range.

Therefore, the doping of S in GaSe crystals could modify their optical properties either in the refractive index or the absorption coefficient in THz range. From the variations of phonon modes in the absorption coefficient spectra, the concentration of S or other elements in the bulk GaSe crystals could be unambiguously detected by the transmission-type THz time-domain spectroscopy. Furthermore, the wavelength-dependent index of refraction shows that the optical properties in THz range are not changed by the slightly S-doping (≦3.0 mass%) in GaSe crystal. Namely, besides the improvement of hardness in GaSe:S (≦3.0 mass%) crystals, their optical properties are kept the same with that of the high-quality GaSe crystals for the applications in THz generation and detection.

(ii) GaSe:Te crystals

Typical profiles of the THz pulses transmitted through the air and samples are shown in Fig. 4-9. The GaSe:Te crystals are illuminated by the THz beam at the focus point. Totally six sorts of the z-cut crystals are employed, one pure GaSe and five in various doping levels $GaSe_{1-x}Te_x$ (x= 0.0006, 0.0012, 0.006, 0.012, and 0.023), i.e. 0.05, 0.1, 0.5, 1.0 and 2.0 mass %; the thickness of them are 1.3, 1.38, 1.22, 1.39, 0.96 and 0.75 mm respectively. The signal beam passes the delay stage which provides the time resolution for THz time-domain spectroscopy. The THz and the femtosecond laser beams are joined to the electro-optic sampling detection part [12].

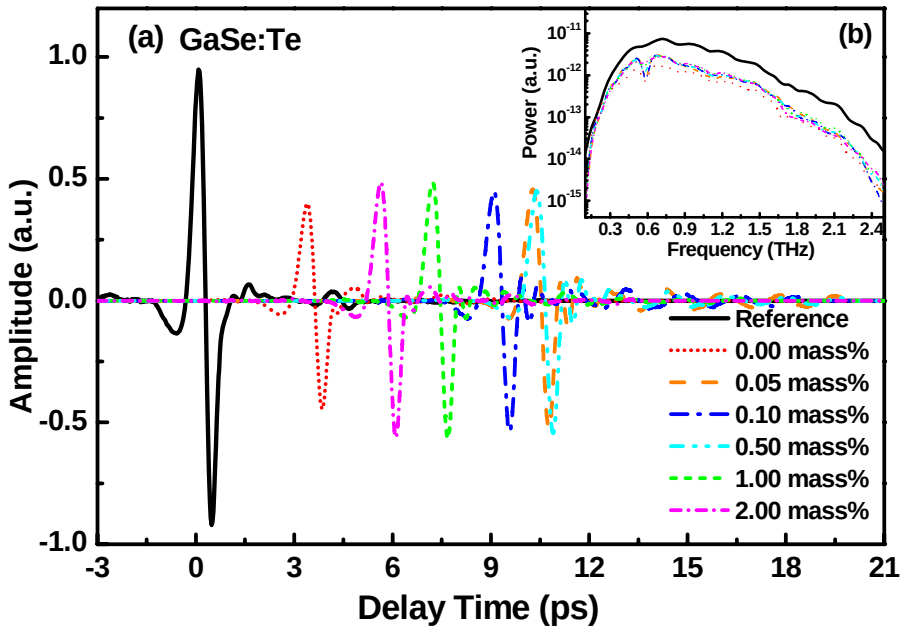

Fig. 4-9 (a) Temporal profiles of the THz pulse transmitted through GaSe:Te crystals and air (thick-solid line). (b) The power spectra of the THz pulse transmitted through GaSe:Te crystals and air (thick-solid line).

The bold black line in Fig. 4-9 shows the typical THz signal with FWHM of about 400 fs at room temperature. After penetrating through samples straightly, a dramatic delay appears due to the optical path length difference between the crystals and the surrounding.

The time domain signal is converted to the frequency domain power spectra P(ω) shown in the inset of Fig. 4-9 within the acceptable S/N region from 0.3 THz to 2.5 THz, which came from the propagation process [20], through the Fast-Fourier Transform. The propagation process can be described by the spectral components, S(ω), which are influenced by the reflectance and the transmittance of both surfaces of a crystal. The second reflection signal locates far from the primitive one, the multi-reflection and the summation effects of Fabry-Perot can be neglected. Additionally, Fig. 4-10 shows the real part of the ordinary refractive indices, which are around 3.22 at low frequency range and rise towards 3.30 due to the Transverse Optical phonon mode oscillation at 6.40 THz [21].

In the transmittance spectra, the absorption deep at 0.58 THz is clearly observed in the inset of Fig. 4-9. Besides, an apparent peak is also observed at the same position (0.58 THz) in absorption coefficient spectra, which is assigned to the so-called rigid layer mode ($E'^{(2)}$) with a rigid unit moving [19]. As increasing the Te-content in GaSe crystals, however, this rigid layer mode gradually shrinks and the other phonon mode ($E''^{(2)}$) correspondingly appears at 1.76 THz which is induced by the Te atom. Both vibrational modes are identified as the $E'^{(2)}$ shear mode and the interlayer vibrational $E''^{(2)}$ shear mode respectively and can be exactly predicated by the first principle calculations [22].

It is proposed that the big Te atoms substitute the Se atoms in high doping level to destroy the integrity of the Se-Ga-Ga-Se layers in GaSe crystals and weaken the rigid layer vibrations. Thus, this absorption spectrum by THz-TDS has the ability to indicate the purity of the GaSe crystals.

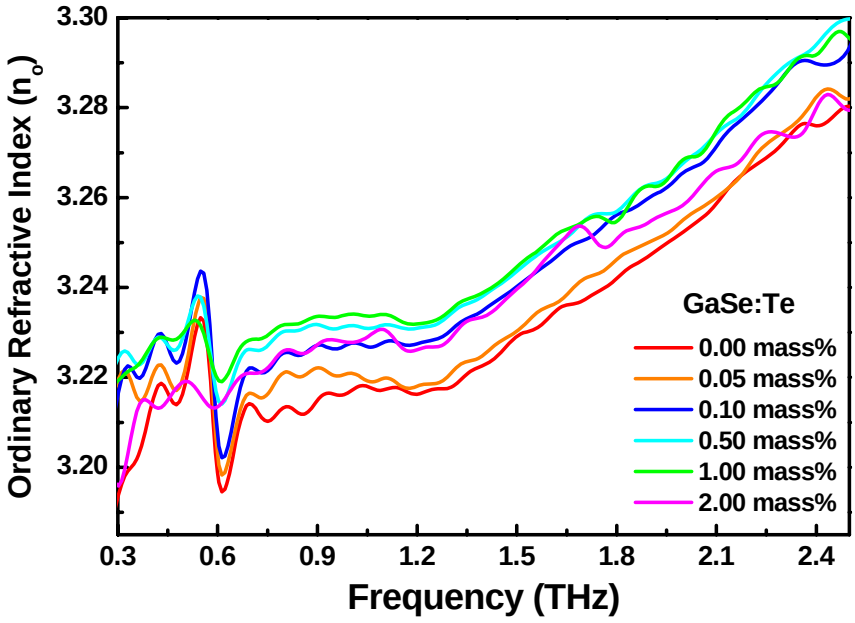

Fig. 4-10 Ordinary reflective index of GaSe:Te crystals.

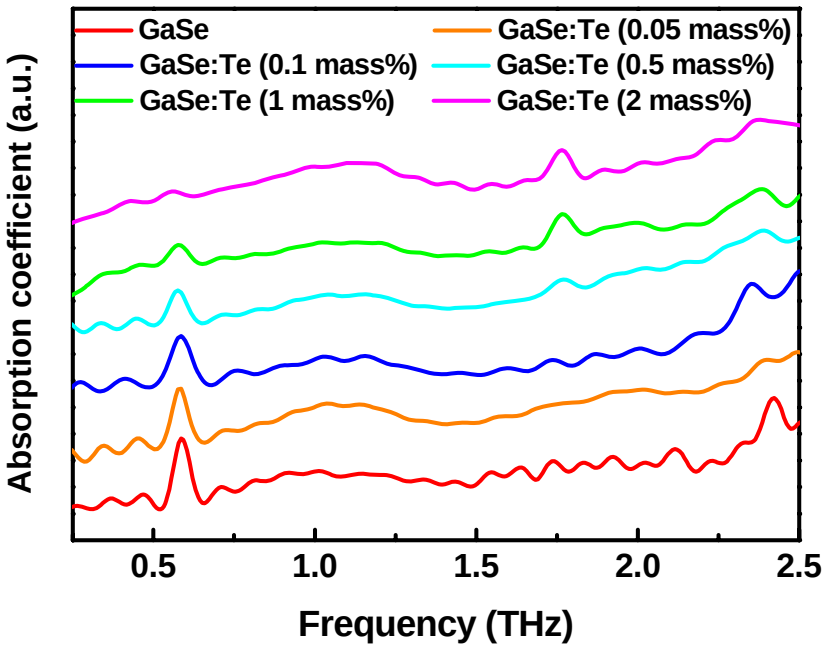

Fig. 4-11 Absorption spectra of GaSe:Te crystals.

4-3. Terahertz generation

As mentioned in Background, GaSe crystals have attractive potential in the mid-IR generation [24]; nevertheless, only few people pay attention on the far-IR (THz) generation. Thus we will focus on the studies of GaSe:S and GaSe:Te crystals in THz generation.

In this study, terahertz generation system has been established as Fig. 4-12. We used the commercial Ti:sapphire oscillator as the light source to provide 800 nm pulses with 35 nm bandwidth and 50 fs pulse duration. The 800 nm laser beam was separated into pump and probe beam by an ultrathin beam spliter. The pump beam was focused on the z-cut GaSe crystals to generate THz. In order to block the 800 nm pump light to reach detection system, a Si wafer was used as a filter (THz transmit/ 800 nm reflect). The transmitted THz pulses were collected and focused on a (110)-oriented ZnTe crystal; meanwhile, the probe beam was also guided by mirrors and focused on the same ZnTe crystal. The Electro-optical sampling technique [12] was adopted to detect THz pulse in time-domain.

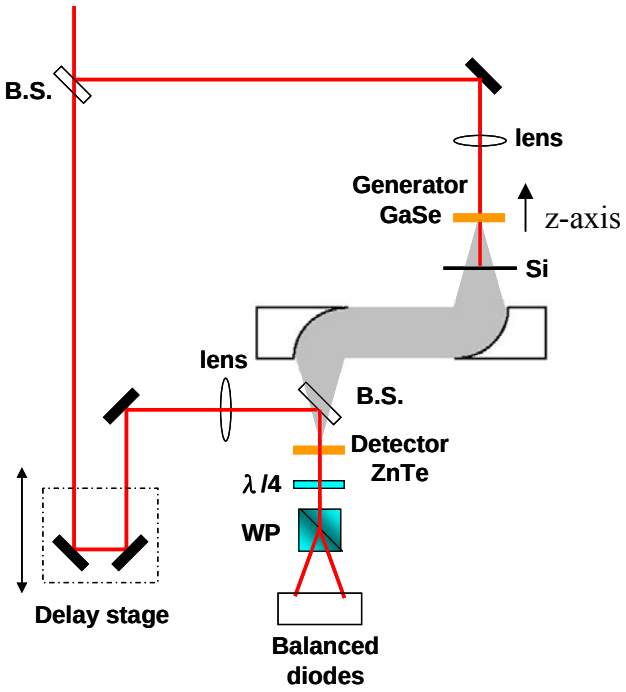

Fig. 4-12 Schematic of THz generation and detection system.

Figure 4-13 shows the φ-dependent electric field of THz in time-domain, where φ is the azimuthal angle (rotating along z-axis of GaSe crystals with normal incident). At φ = 0°, no THz signals was detected. As increasing the φ angle, the amplitude of THz signal increases with negative sign and then reach maximum at φ = 30°. While φ > 30°, the amplitude of THz signal decrease again and passes zero at φ = 60°. If the φ angle was increased again, the amplitude of THz signal will increase and then decrease but with opposite sign. While the GaSe crystal was rotated with 360°, a sinusoidal variation can be clearly observed in the inset of Fig. 4-13. Additionally, if we take the absolute value of the sinusoidal curve in the inset of Fig. 4-13, it will clearly present the six-fold symmetry which is due to the hexagonal structure of GaSe crystals. This further implies that the optical rectification is responsible for the THz generation in GaSe crystals.

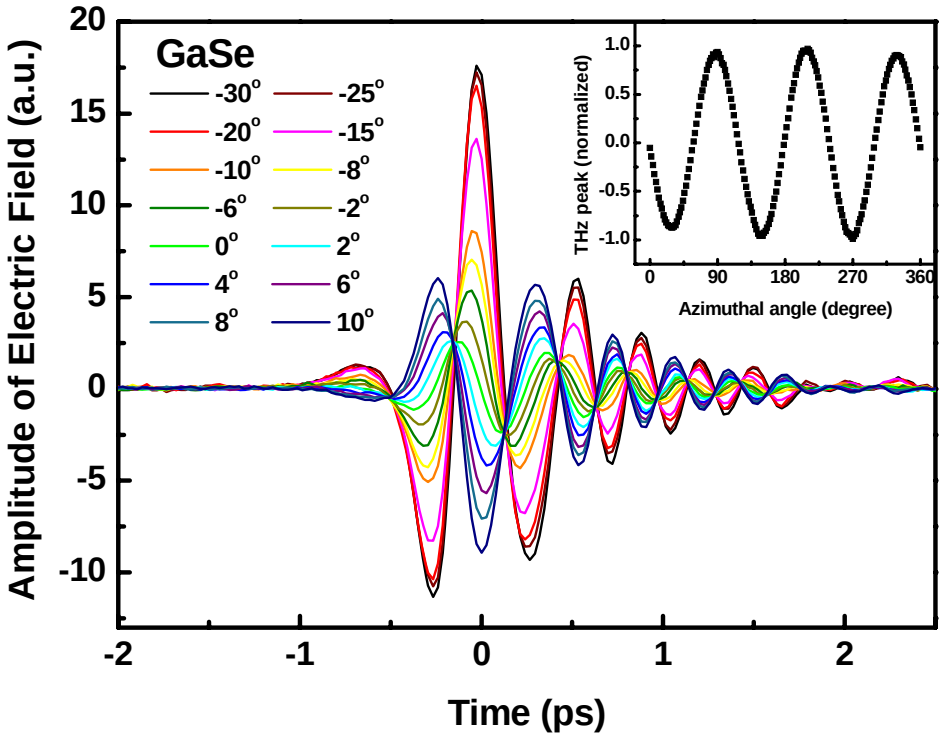

Fig. 4-13 The THz time-domain waveforms at various azimuthal angles rotating along the z-axis of GaSe crystals. Inset: the amplitude of the THz pulse as a function of φ angle.

Moreover, if we fix the φ angle at 90° and change the incident angle θ between the incident direction of laser beam and z-axis of GaSe crystals, we only observe the variation of THz intensity without spectra change as shown in Fig. 4-14. This indicates that the mechanism of phase match should not involve in this THz generation process. Thus, the THz generated from GaSe crystals is directly from the mechanism of optical rectification.

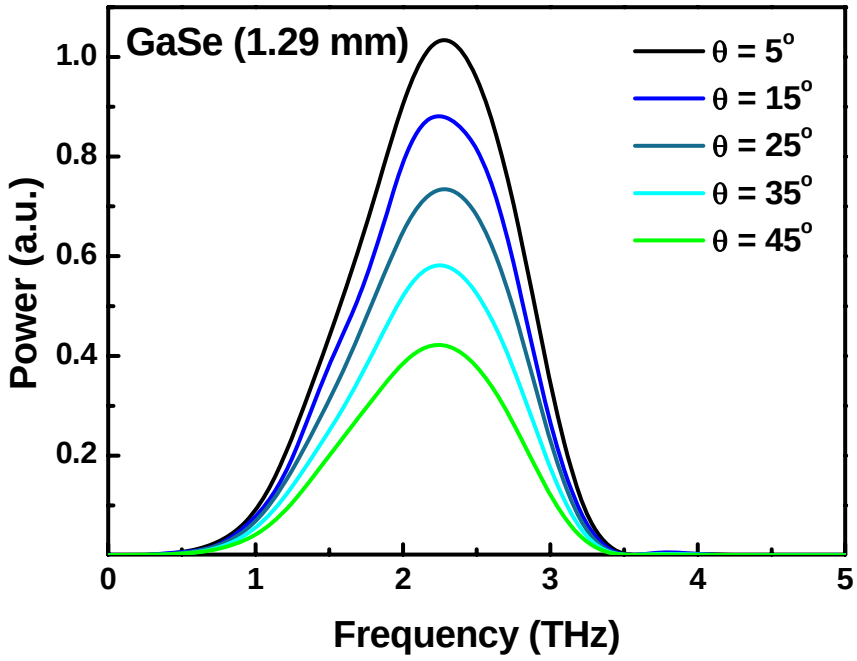

Fig. 4-14 The spectra of THz generated from GaSe crystals at various θ angles.

(i) GaSe:S crystals

Figure 4-15(a) shows the THz electric field in time-domain from various GaSe:S crystals. With different thickness and index of reflection, the THz signals of different S-doped GaSe crystals were measured at different delay time. By FFT, the time-domain THz signal in Fig. 4-15(a) can be transfer to frequency domain as shown in Fig. 4-15(b). Most central frequency of these THz spectra locates at around 2 THz with the bandwidth of ~1.5 THz.

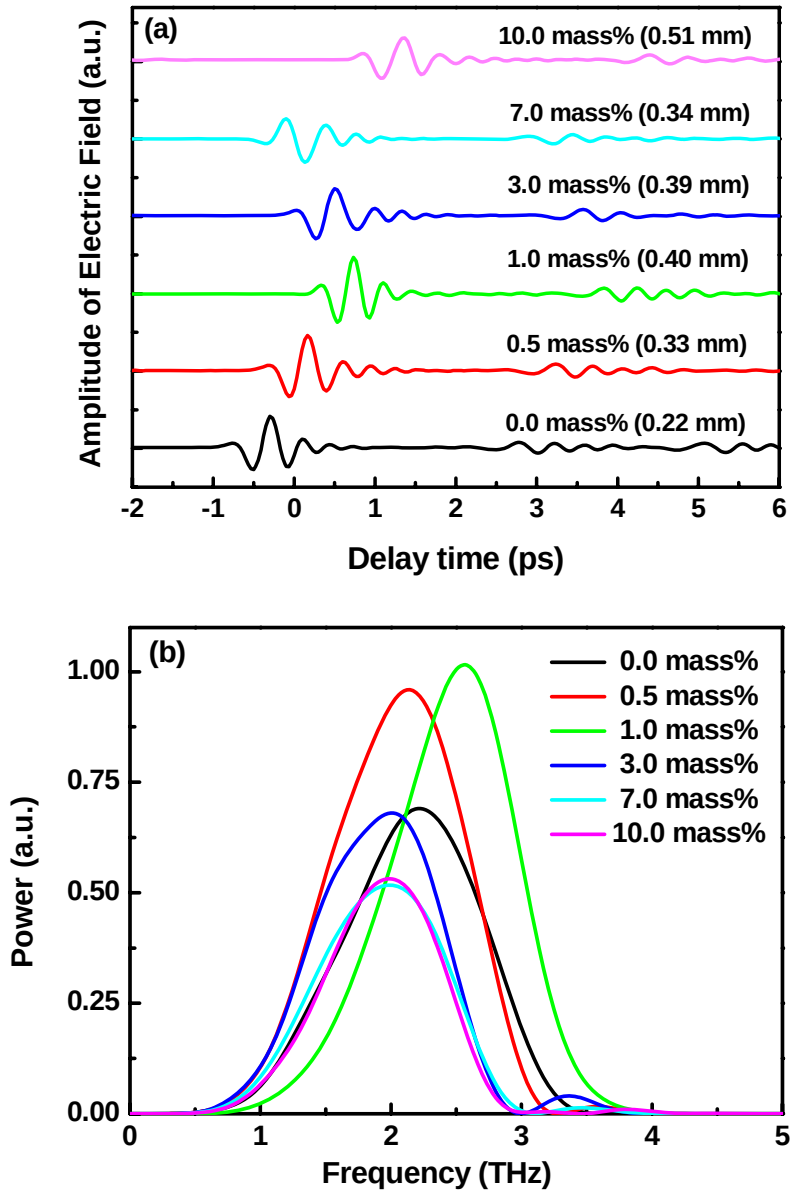

Fig. 4-15 (a)The THz electric field waveforms in time-domain and (b)spectra from various GaSe:S crystals.

In order to analyze the evolution of THz generation efficiency and central frequency at various S concentrations, we plotted all of the data extracted from Fig. 4-15 in Fig. 4-16 together. In slightly S doping concentration (S < 2 mass%), the amplitude of THz electric field is larger than that of pure GaSe crystals (Black triangle point in Fig. 4-16). However, the amplitude of THz electric field decreases when the S concentration > 2 mass%. This may be due to the higher crystals quality in slightly S-doping.

In heavy S-doping cases, the low THz generation efficiency is due to the appearance of GaS with low nonlinear effect. Moreover, the central frequency of THz signal gradually decreases as increasing the S concentrations.

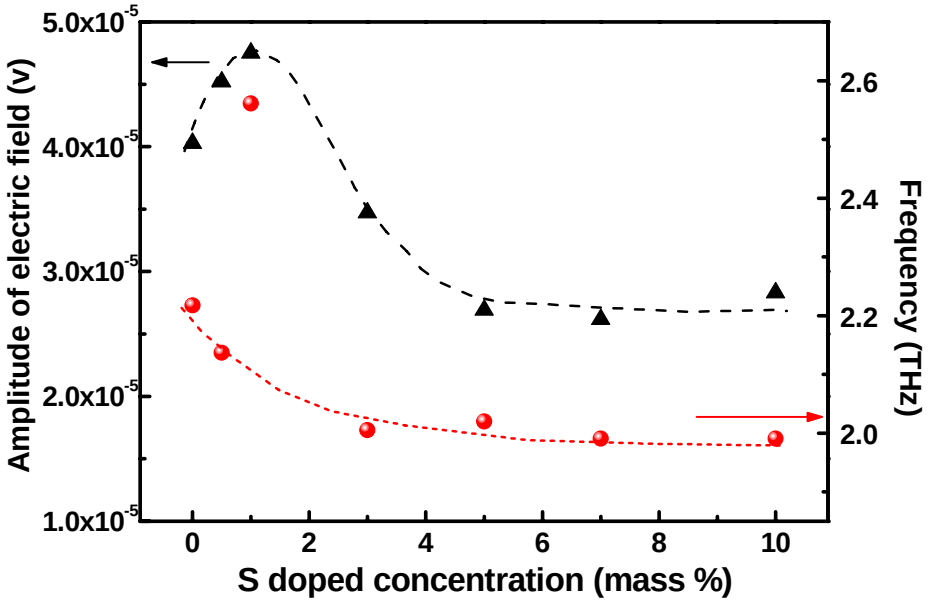

Fig. 4-16 The amplitude of THz electric field and the central frequency of FFT spectra as a function of S concentration.

(ii) GaSe:Te crystals

Figure 4-17(a) shows the THz electric field in time-domain from various GaSe:Te crystals. With different thickness and index of reflection, the THz signals of different Te-doped GaSe crystals were measured at different delay time. By FFT, the time-domain THz signal in Fig. 4-17(a) can be transfer to frequency domain as shown in Fig. 4-17(b). Most central frequency of these THz spectra locates at around 2.2 THz with the bandwidth of ~1.5 THz.

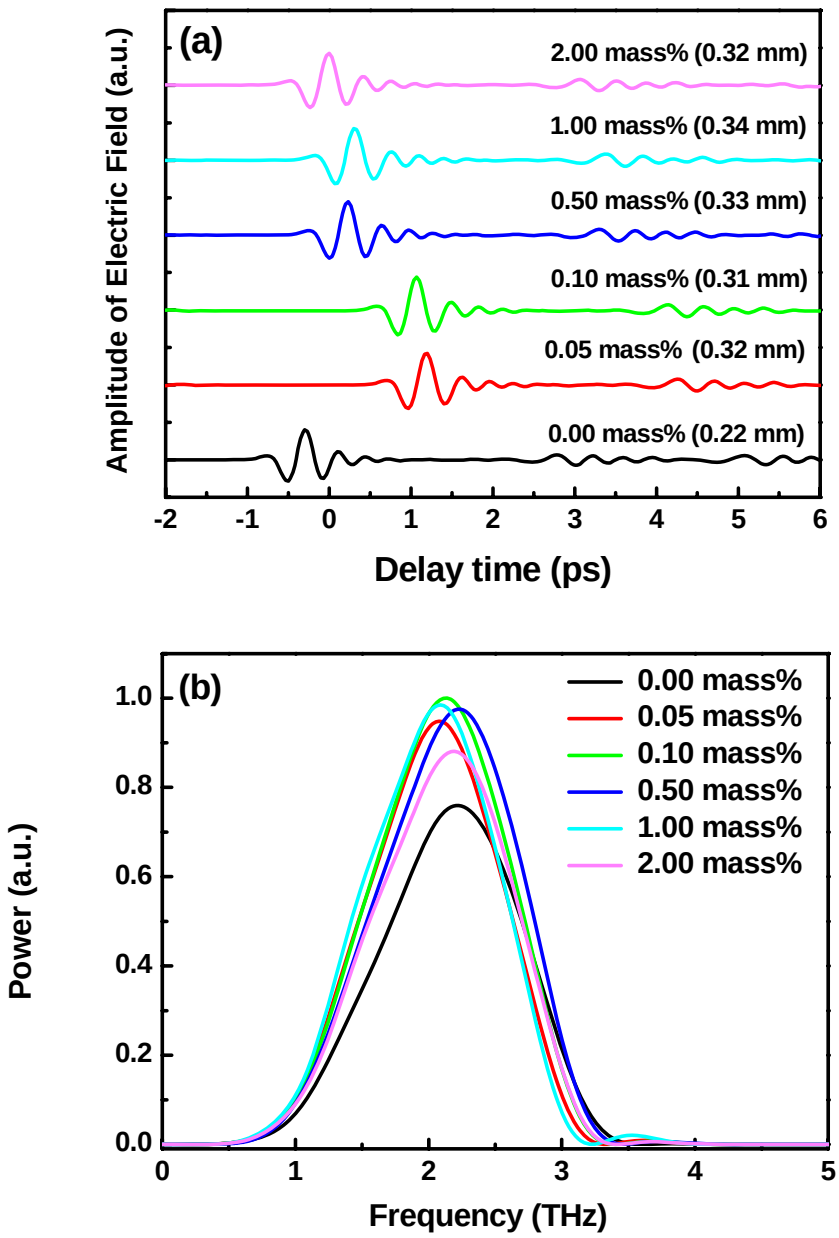

Fig. 4-17 (a)The THz electric field waveforms in time-domain and (b)spectra from various GaSe:Te crystals.

In order to analyze the evolution of THz generation efficiency and central frequency at various Te concentrations, we plotted all of the data extracted from Fig. 4-17 in Fig. 4-18 together. In slightly Te doping concentration (Te < 0.1 mass%), the amplitude of THz electric field is larger than that of pure GaSe crystals (Black triangle point in Fig. 4-18). This may be due to the stronger nonlinear effect caused by the heavier Te atom. However, the amplitude of THz electric field decreases when the Te

concentration > 0.1 mass% owing to the larger size of Te atom to distort the GaSe lattice structure and reduce the nonlinear effect. Moreover, the central frequency of THz signal almost keeps a constant as increasing the Te concentrations.

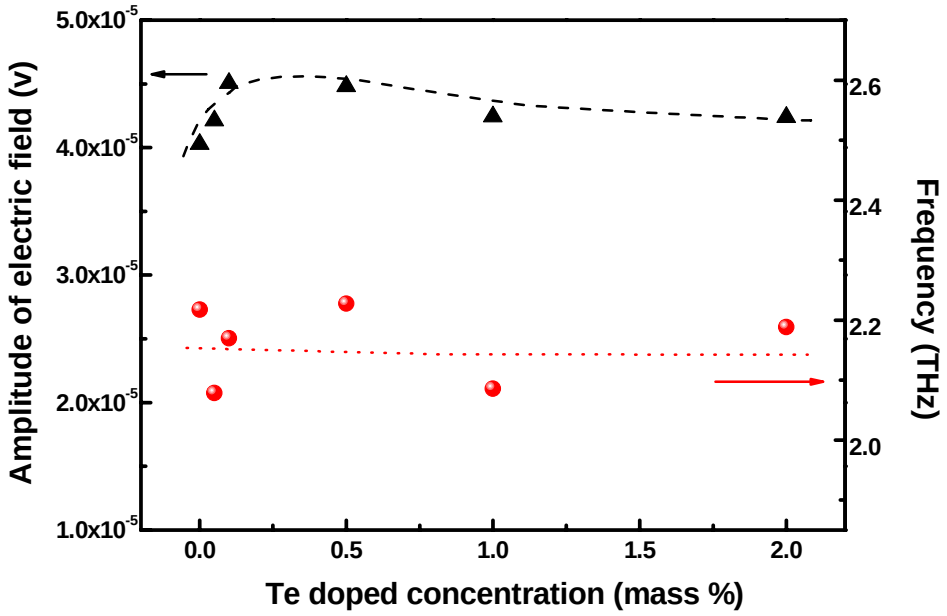

Fig. 4-18 The amplitude of THz electric field and the central frequency of FFT spectra as a function of S concentration.

5. Summary:

In this Taiwan-Russia cooperation project, we have successfully prepared the GaSe:S and GaSe:Te single crystals in Tomsk, Russia and finished the optical measurements in Taiwan. At first, the mechanical properties of GaSe crystals, e.g. the hardness, have been enhanced by S-doping. Besides, the S-doping indeed change the GaSe lattice structure and even form the GaS compound in heavy S-doping, which were observed by the Raman spectra. For the electric properties, the carrier concentration, mobility, and conductivity in slightly S-doped GaSe crystals are higher than the pure GaSe crystals. However, these electric parameters reduce almost one order of magnitude in the heavy S-doped GaSe crystals. Moreover, both GaSe:S and GaSe:S can be used to generate THz radiation at ~2 THz with the bandwidth of 1.5 THz by femtosecond laser pulses. For the GaSe:Te crystals, the THz generation efficiency have been improved due to the higher nonlinear effect. For instance, the THz radiation was enhanced by 12.5% in GaSe:Te with 0.1 mass%. Therefore, we not only well prepared the GaSe:S and GaSe:Te crystals, but also finished the studies of the mechanical, electric, and optical properties. Furthermore, we found the THz radiation in 2 THz region can be efficiently enhanced in GaSe:Te crystals.

6. References:

[1] The cover picture of Rensselear Magazine, http://www.rpi.edu/change/zhang.html.

[2] D. H. Auston Appl. Phys. Lett. **26**, 101 (1975).

[3] A. G. Davies *et al.*, Phys. Med. Biol. **47**, 3679 (2002).

[4] M. Tani *et al.*, Meas. Sci. Technol. **13**, 1739 (2002).

[5] X.-C. Zhang *et al*., Appl. Phys. Lett. **56**, 1011 (1990).

[6] F. Klappenberger *et al*., Int. J. of Infrar. and Millim. Waves **24**, 1405 (2003).

[7] G. L. Carr *et al*., Nature **420**, 153 (2002).

[8] Ruedeger Koehler *et al*., Nature **417**, 156 (2002).

[9] W. Shi *et al*., Appl. Phys. Lett. **84**, 1635 (2004).

[10] W. Shi *et al*., Opt. Commun. **233**, 183 (2004).

[11] M. Hayek *et al*., Phys. Rev. **B 8**, 2772 (1973).

[12] Q. Wu *et al*., Appl. Phys. Lett. **67**, 3523-3525 (1995).

[13] B. L. Yu *et al*., Appl. Phys. Lett. **87**, 182104 (2005).

[14] C. H. Ho *et al*., J. Cryst. Growth. **279**, 321-328 (2005).

[15] C. H. Ho *et al*., Soild State Comm. **136**, 591-594 (2008).

[16] Yu. M. Andreev *et al*., Mater. Sci. and Eng. B **128**, 205-210 (2006).

[17] C. Manfredotti *et al*., Phys. Stat. Sol. (a) **48**, 293 (1978).

[18] H. Yoshida *et al*., Phys. Stat. Sol. (B) **59**, 655-666 (1973).

[19] C. W. Chen *et al*., J. Opt.Soc. Am. B **26**, 58-65 (2009).

[20] L. Duvillaret *et al*., IEEE J. Sel. Top. Quan. Elec., **2**, 739-746 (1996).

[21] B.Tatian, Appl. Opt. **23**, 4477-4485 (1984).

[22] T. F. Huang, NCTU, GN0697410303 (2010).

7. **Self-evaluation:**

國科會補助專題研究計畫成果報告自評表

請就研究內容與原計畫相符程度、達成預期目標情況、研究成果之學術或應用價值（簡要敘述成果所代表之意義、價值、影響或進一步發展之可能性）、是否適合在學術期刊發表或申請專利、主要發現或其他有關價值等，作一綜合評估。

1. 請就研究內容與原計畫相符程度、達成預期目標情況作一綜合評估

■ 達成目標

□ 未達成目標（請說明，以 100 字為限）

□ 實驗失敗

□ 因故實驗中斷

□ 其他原因

說明：

2. 研究成果在學術期刊發表或申請專利等情形：

論文：■已發表 □未發表之文稿 ■撰寫中 □無

專利：□已獲得 □申請中 ■無

技轉：□已技轉 □洽談中 ■無

其他：（以 100 字為限）

3. 請依學術成就、技術創新、社會影響等方面，評估研究成果之學術或應用價值（簡要敘述成果所代表之意義、價值、影響或進一步發展之可能性）（以 500 字為限）

本台俄國際合作計畫是由俄方提供不同摻雜之硒化鎵晶體，由我方進行兆赫波之產生與特性分析。因為本計劃之執行，俄方成功成長各式摻雜之硒化鎵晶體，我方則成功建立各種兆赫波產生之系統與技術。雙方亦一起發表學術論文於國際期刊，目前仍有數篇論文正在審查與撰稿中。在適當的摻雜下，的確改善了硒化鎵晶體的機械與物理特性，也提升了兆赫波的產生效率，這對日後兆赫波的應用奠定了良好的基礎及提供了重要的依據。除此之外，透過學術交流與互訪，加深我方對俄羅斯社經文化的認識與了解，當然，我們也把握機會將台灣文化介紹給俄羅斯的朋友們。

8. Publication list:

1. **C. W. Luo***, Y. Q. Yang, I. T. Mak, Y. H. Chang, K. H. Wu and T. Kobayashi, 2008 February, *A widely tunable dual-wavelength CW Ti:sapphire laser with collinear output*, Opt. Express 16, 3305 ~ 3309.

   SCI, NSC95-2112-M-009-011-MY3, NSC96-2923-M-009-001-MY3

2. T. H. Lin*, C. C. Hsieh, H. C. Shih, **C. W. Luo**, T. M. Uen, K. H. Wu, J. Y. Juang*, J.-Y. Lin, C.-H. Hsu and S. J. Liu, 2008 March, *Anomalous magnetic ordering in b-axis-oriented orthorhombic $HoMnO_3$ thin films*, Appl. Phys. Lett. 92, 132503-1~132503-3.

   SCI, NSC95-2112-M-009-011-MY3, NSC96-2923-M-009-001-MY3

3. Bo-An Tsai, Yao-Jen Lee*, Hsin-Yi Peng, Pei-Jer Tzenf, **Chih-Wei Luo**, and Kuei-Shu Chang-Liao 2008 April, *Using Spike-Anneal to Reduce Interfacial Layer Thickness and Leakage Current in Metal-Oxide-Semiconductor Device with TaN/Atomic Layer Deposition-Grown HfAlO/Chemical Oxide/Si Structure*, Jpn. J. Appl. Phys. 47, 2438~2441.

   SCI, NSC95-2112-M-009-011-MY3, NSC96-2923-M-009-001-MY3

4. C. C. Hsieh*, T. H. Lin, H. C. Shih, C.-H. Hsu, **C. W. Luo**, J.-Y. Lin, K. H. Wu, T. M. Uen and J. Y. Juang, 2008 November, *Magnetic ordering anisotropy in epitaxial orthorhombic multiferroic $YMnO_3$ films*, J. Appl. Phys., 104, 103912-1~103912-7.

   SCI, NSC95-2112-M-009-011-MY3, NSC96-2923-M-009-001-MY3

5. **C.W. Luo***, C. C. Lee, C. H. Li, H. C. Shih, Y.-J. Chen, C. C. Hsieh, C. H. Su, W. Y. Tzeng, K. H.Wu, J. Y. Juang, T. M. Uen, S. P. Chen, J.-Y. Lin, T. Kobayashi, 2008 December, *Ordered YBCO sub-micron array structures induced by pulsed femtosecond laser irradiation*, Opt. Express 16, 20610 ~ 20616.

   SCI, NSC95-2112-M-009-011-MY3, NSC96-2923-M-009-001-MY3

6. Y.C. Tsai*, W.J. Chang, C.C. Hsieh, **C.W. Luo**, K.H. Wu, T.M. Uen, J.Y. Juang, J.-Y. Lin,

2009 January, *Phase separation and persistent magnetic memory effect in* $La_{0.625}Ca_{0.375}MnO_3$ *and* $La_{0.375}Pr_{0.25}Ca_{0.375}MnO_3$ *films*, J. Appl. Phys., 105, 013705-1~013705-5.

SCI, NSC95-2112-M-009-011-MY3, NSC96-2923-M-009-001-MY3

7. T.H. Lin*, H.C. Shih, C.C. Hsieh, **C.W. Luo**, J.-Y. Lin, J.L. Her, H.D. Yang, K.H. Wu, T.M. Uen, J.Y. Juang, 2009 January, *Strain-induced effects on magnetic ordering and magneto-capacitance in orthorhombic HoMnO3 thin films*, J PHYS-CONDENS MAT, 21, 026013-1~026013-5.

SCI, NSC95-2112-M-009-011-MY3, NSC96-2923-M-009-001-MY3

8. K. H. Wu*, T. Y. Hsu, H. C. Shih, Y. J. Chen, **C. W. Luo**, T. M. Uen, J.-Y. Lin, J.Y. Juang, T. Kobayashi, 2009 February, *Ultrafast Optical Probes of Polaron Dynamics in* $La_{0.7}Ca_{0.3}MnO_3$ *Thin Films*, J. Appl. Phys., 105, 043901-1~043901-5.

SCI, NSC95-2112-M-009-011-MY3, NSC96-2923-M-009-001-MY3

9. **C. W. Luo***, Y. T. Wang, F. W. Chen, H. C. Shih, and T. Kobayashi, 2009 June, *Eliminate coherence spike in reflection-type pump-probe measurements*, Opt. Express **17**, 11321~11327.

✦It has been selected for the August 2009 issue of Virtual Journal of Ultrafast Science

SCI, NSC95-2112-M-009-011-MY3, NSC96-2923-M-009-001-MY3

10. J. W. Chou, Kao-Chin Lin, Yao-Jen Lee, Chi-Tsu Yuan, Fu-Kuo Hsueh, Hsun-Chuan Shih, Wen-Chung Fan, **Chih-Wei Luo**, Ming-Chieh Lin, Wu-Ching Chou, and Der-San Chuu*, 2009 July, *Observation of the Localized Surface Plasmons in Spatially Controlled Array Structures*, Nanotechnology **20**, 305202-1~ 305202-6.

SCI, NSC95-2112-M-009-011-MY3, NSC96-2923-M-009-001-MY3

11. H. C. Shih*, T. H. Lin, **C. W. Luo***, J.-Y. Lin, T. M. Uen, J. Y. Juang, K. H. Wu, J. M. Lee, J. M. Chen, and T. Kobayashi, 2009 July, *Magnetization dynamics and* Mn^{3+} *d-d*

excitation in hexagonal $HoMnO_3$ revealed by wavelength-tunable time-resolved femtosecond spectroscopy, Phys. Rev. **B 80**, 024427-1~024427-5.

✦It has been selected for the August 2009 issue of Virtual Journal of Ultrafast Science

SCI, NSC95-2112-M-009-011-MY3, NSC96-2923-M-009-001-MY3

12. J W Chou, K C Lin, Y T Tang, F K Hsueh, Yao-Jen Lee, **C W Luo**, Y N Chen, C T Yuan, Hsun-Chuan Shih, W C Fan, M C Lin, W C Chou, and Der-San Chuu*, 2009 September, *Observation of the Localized Surface Plasmons in Spatially Controlled Array Structures*, Nanotechnology **20**, 415201-1 ~ 415201-5.

SCI, NSC95-2112-M-009-011-MY3, NSC96-2923-M-009-001-MY3

13. T. H. Lin*, C. C. Hsieh, **C. W. Luo**, J.-Y. Lin, C. P. Sun, H. D. Yang, C.-H. Hsu, Y. H. Chu, K. H. Wu, T. M. Uen, and J. Y. Juang*, 2009 November, *Magnetism-induced ferroelectric polarization in the c-axis-oriented orthorhombic HoMnO3 thin films*, J. Appl. Phys. **106,** 103923-1 ~ 103923-4.

SCI, NSC95-2112-M-009-011-MY3, NSC96-2923-M-009-001-MY3

14. K. H. Wu*, I. C. Gou, **C. W. Luo**, T. M. Uen, J.-Y. Lin, J.Y. Juang, C. K. Chen, J. M. Lee and J. M. Chen, 2010 January, *Anisotropic electronic structure in single crystalline orthorhombic $TbMnO_3$ Thin Films*, Thin Solid Films 5**18,** 2275~2279.

SCI, NSC95-2112-M-009-011-MY3, NSC96-2923-M-009-001-MY3

15. **C. W. Luo***, T. C. Huang, M. T. Chiang, K. H. Wu, J. Y. Juang, J.-Y. Lin, and T. M. Uen, 2010 January, *Anisotropic ultrafast dynamics of quasiparticles on CuO_2 planes of $Y_{0.7}Ca_{0.3}Ba_2Cu_3O_{7-\delta}$*, J. Supercond. Nov. Magn. **23,** 781~784.

SCI, NSC95-2112-M-009-011-MY3, NSC96-2923-M-009-001-MY3

16. **C. W. Luo***, H. P. Lo, C. H. Su, I. S. Wu, Y.-J. Chen, K. H. Wu, J.-Y. Lin, T. M. Uen, J. Y. Juang, and T. Kobayashi, 2010 September, *Doping dependence of the ultrafast electronic dynamics of $Y_{1-x}Pr_xBa_2Cu_3O_7$ thin-film superconductors from femtosecond optical spectroscopy*, Phys. Rev. **B 82,** 104512-1~104512-5.

SCI, NSC95-2112-M-009-011-MY3, NSC96-2923-M-009-001-MY3

17. Y. H. Lee*, A. Yabushita, C. S. Hsu, S. H. Yang, I. Iwakura, **C. W. Luo**, K. H. Wu, and T. Kobayashi, 2010 September, *Ultrafast relaxation dynamics of photoexcitations in poly(3-hexylthiophene) for the determination of the defect concentration*, Chem. Phys. Lett. **498,** 71~76.

SCI, NSC95-2112-M-009-011-MY3, NSC96-2923-M-009-001-MY3